

The Mass Assembly Histories of Galaxies of Various Morphologies in the GOODS Fields

Kevin Bundy¹, Richard S. Ellis¹, Christopher J. Conselice¹

kbundy@astro.caltech.edu, rse@astro.caltech.edu, cc@astro.caltech.edu

ABSTRACT

We present an analysis of the growth of stellar mass with cosmic time partitioned according to galaxy morphology. Using a well-defined catalog of 2150 galaxies based, in part, on archival data in the Great Observatories Origins Deep Survey (GOODS) fields, we assign morphological types in three broad classes (Ellipticals, Spirals, Peculiar/Irregulars) to a limit of $z_{AB}=22.5$ and make the resulting catalog publicly available. Utilizing 893 spectroscopic redshifts, supplemented by 1013 determined photometrically, we combine optical photometry from the GOODS catalog and deep K_s -band imaging to assign stellar masses to each galaxy in our sample. We find little evolution in the form of the galaxy stellar mass function from $z \sim 1$ to $z = 0$, especially at the high mass end where our results are most robust. Although the population of massive galaxies is relatively well established at $z \sim 1$, its morphological mix continues to change, with an increasing proportion of early-type galaxies at later times. By constructing type-dependent stellar mass functions, we show that in each of three redshift intervals, E/S0's dominate the higher mass population, while spirals are favored at lower masses. This transition occurs at a stellar mass of $2\text{--}3 \times 10^{10} M_\odot$ at $z \sim 0.3$ (similar to local studies) but there is evidence that the relevant mass scale moves to higher mass at earlier epochs. Such evolution may represent the morphological extension of the “downsizing” phenomenon, in which the most massive galaxies stop forming stars first, with lower mass galaxies becoming quiescent later. We infer that more massive galaxies evolve into spheroidal systems at earlier times, and that this morphological transformation may only be completed 1–2 Gyr after the galaxies emerge from their active star forming phase. We discuss several lines of evidence suggesting that merging may play a key role in generating this pattern of evolution.

Subject headings: cosmology: observations, galaxies: formation, galaxies: evolution, morphologies

¹105–24 Caltech, 1201 E. California Blvd., Pasadena, CA 91125

1. Introduction

Great progress has been made in recent years in defining the star formation history of galaxies (Madau et al. 1996; Blain et al. 1999). The combination of statistically complete redshift surveys (Lilly et al. 1995; Ellis et al. 1996; Steidel et al. 1999; Chapman et al. 2003) and various diagnostics of star formation (UV continua, recombination lines and sub-mm emission) has enabled determinations of the co-moving star formation (SF) density at various redshifts whose rise and decline around $z \simeq 2$ points to the epoch when most stars were born (e.g. Rudnick et al. 2003; Bouwens et al. 2003; Bunker et al. 2004). Many details remain to be resolved, for example in reconciling different estimators of star formation (e.g. Sullivan et al. 2004) and the corrections for dust extinction. In addition, recent theoretical work including both numerical simulations and semi-analytic modeling is in some confusion as to the expected result (e.g. Baugh et al. 1998; Somerville et al. 2001; Nagamine et al. 2004).

An independent approach to understanding how galaxies form is to conduct a census of galaxies *after* their most active phases and to track their growing stellar masses. The co-moving stellar mass density at a given redshift should represent the integral of the previously-discussed SF density to that epoch, culminating in its locally-determined value (Fukugita et al. 1998). Unlike the star formation rate (SFR), the stellar mass of a galaxy is less transient and can act as a valuable tracer for evolutionary deductions.

Further insight is gained by tracing the integrated growth in stellar mass of different populations. For example, the rapid decline with time in the SF density over $0 < z < 1$ (Lilly et al. 1996; Fall et al. 1996) appears to result from the demise of an abundant population of star forming, irregular galaxies (Glazebrook et al. 1995; Abraham et al. 1996; Brinchmann et al. 1998). By considering the declining stellar mass density associated with irregular galaxies, Brinchmann & Ellis (2000) suggested that these sources transform, either by mergers or other means, into the slowly growing mass identified with regular ellipticals and spirals.

In a complementary fashion, the recent completion of large infrared surveys like K20 (Cimatti et al. 2002) and MUNICS (Drory et al. 2001) has traced the distribution in mass of the most massive galaxies out to $z \sim 2$ (Fontana et al. 2004; Drory et al. 2004). These and other studies find a decrease in the overall normalization of the combined galaxy stellar mass function with redshift. Fontana et al. (2004) find very little evolution in the shape of the combined mass function out to $z \sim 1$. Drory et al. (2004), in contrast, argue for a stronger evolution out to $z \sim 1$ based on a decrease in the characteristic mass and steepening of the faint-end slope. The MUNICS survey, though extensive in size, relies primarily on photometric redshifts and, at $K \lesssim 18.7$ (Vega), probes a limited mass range. The deeper K20 survey, on the other hand, utilizes primarily spectroscopic redshifts, but is much smaller

and suffers more from cosmic variance.

With sufficient data, it is possible to combine these earlier approaches, which concentrated on either volume-integrated quantities of separate populations or the mass distribution of combined galaxy types, and construct the stellar mass functions of individual populations. At $z = 0$, Bell et al. (2003) have used measurements of concentration and color in the Sloan Digital Sky Survey (SDSS) to classify galaxies as early or late type and derived separate mass functions for each, demonstrating that early-types dominate at higher masses. Baldry et al. (2004) use the bimodal color distribution observed in SDSS to separate early from late populations and find similar results. At higher redshifts, Fontana et al. (2004) were the first to examine type-dependent mass functions and divided their sample based on spectral type, finding some evidence for bimodality.

The public availability of ACS images and photometry in the Great Observatories Origins Deep Survey (GOODS, Giavalisco et al. 2004) together with spectroscopic redshifts (e.g. Wirth et al. 2004; Le Fèvre et al. 2004) provides a new opportunity for making progress at $z \sim 1$. With the addition of infrared photometry, it is possible to characterize the mass functions of separate and well defined *morphological* populations, although the small size of the GOODS fields makes cosmic variance one of the primary sources of uncertainty. It is therefore advantageous to combine the two GOODS fields, even though GOODS-N has the benefit of roughly twice as many spectroscopic redshifts as GOODS-S. With the various datasets available in GOODS, we can begin mapping out the mass assembly history responsible for the origin of the Hubble Sequence as well as understanding the physical processes that drive this assembly.

A plan of the paper follows. In §2 we discuss the essential ingredients: the infrared data, including new K_s -band imaging of the GOODS-N field undertaken with the Hale 5m reflector at Palomar; visual morphologies of the ACS-selected galaxies in GOODS; and spectroscopic and photometric redshifts. In §3 we introduce our method for measuring stellar masses for galaxies of known redshift based on infrared and optical photometry. In §4 we discuss important issues of completeness and selection effects in the sample. In §5 we present the methods and results of our analysis of the stellar mass functions and the integrated mass density of various morphological populations. We summarize and conclude in §7. Throughout, we assume a cosmological model with $\Omega_M = 0.3$, $\Omega_\Lambda = 0.7$ and $H_0 = 100h$ km s⁻¹ Mpc⁻¹.

2. Data

This study relies on the combination of many different datasets in the GOODS fields including infrared observations, spectroscopic and photometric redshifts, and HST morphologies.

2.1. Infrared Imaging

Because deep infrared data is not publicly available in GOODS-N, we carried out K_s -band imaging of the GOODS-N field in three overlapping pointings $8'6$ on a side, using the Wide-field Infrared Camera (WIRC, Wilson et al. 2003) on the Hale 5m telescope at Palomar Observatory. The observations were made in November 2002, January 2003, and April 2003 under slightly different conditions. The total integration times for each of the sub-fields of 15ks, 13ks, and 5.6ks account for the different observing conditions so that the final depth in each pointing is similar. Mosaics of numerous coadditions of a sequence of 4×30 second exposures were taken in a non-repeating pattern of roughly $7''0$ dithers and processed using a double-pass reduction pipeline we developed specifically for WIRC. The individual observations were combined by applying weights based on the seeing, transparency, and background for each observation. The final data quality is excellent, with average FWHM values for stars in the WIRC images of $0''.85$ for the first two fields and $1''.0$ for the third. Because the WIRC camera field is fixed North-South and cannot be rotated and only three positions were imaged, the overlap with the GOODS-N region is only $\sim 70\%$.

The WIRC images were calibrated by observing standard stars during photometric conditions and checked with comparisons to published K-band photometry from Franceschini et al. (1998). A comparison for relatively bright stars in each field was also made with 2MASS. Photometric errors and the image depth were estimated by randomly inserting fake objects of known magnitude into each image and then recovering them with the same detection parameters used for real objects. The inserted objects were given Gaussian profiles with a FWHM of $1''.3$ to approximate the shape of slightly extended, distant galaxies. The resulting 80% completeness values in the K_s -band are 22.5, 22.8, and 22.4 AB, which are similar to the $5\text{-}\sigma$ detection limit in each image.

Infrared imaging is publicly available for GOODS-S. We utilized K_s -band data taken with the SOFI instrument on the NTT because it is similar in depth and resolution to the Palomar observations. The SOFI data reach $K_s < 22.5$ (AB, $5\text{-}\sigma$) with stellar FWHM values less than $1''.0$ on average. Detailed information on the SOFI observations can be found in Vandame et al. (2001).

For the infrared imaging in both GOODS fields, we used SExtractor (Bertin & Arnouts 1996) to make a K-band catalog, limited to $K_s = 22.4$ (AB), and for total magnitudes we use the SExtractor Kron estimate. We do not adjust the Kron magnitude to account for missing light in extended sources. The optical-infrared color measurements, which are used for estimating photometric redshifts and stellar masses, are determined from $1''0$ radius aperture photometry. In the case of the infrared data, these measurements are made by SExtractor. They are then compared to the catalog of optical ACS $BViz$ $1''0$ photometry as tabulated by the GOODS team (Giavalisco et al. 2004).

2.2. ACS Morphologies

Based on version 1.0 HST/ACS data released by the GOODS team (Giavalisco et al. 2004), a z -selected catalog was constructed with a magnitude limit of $z_{AB} = 22.5$, where reliable visual morphological classification was deemed possible. The resulting sample of 2978 objects spread over both GOODS fields was inspected visually by one of us (RSE) who classified each object (using techniques discussed in detail by Brinchmann et al. 1998) according to the following scale: -2=Star, -1=Compact, 0=E, 1=E/S0, 2=S0, 3=Sab, 4=S, 5=Scd, 6=Irr, 7=Unclass, 8=Merger, 9=Fault. Following Brinchmann & Ellis (2000), we divide these classes into three broad categories: ‘E/S0’ combines classes 0, 1, and 2 and contains 627 galaxies; ‘Spirals’ combines classes 3, 4, and 5 and contains 1265 galaxies; and ‘Peculiar/Irregular’ comprises classes 6, 7 and 8 and contains 562 galaxies. The morphological catalog is publicly available at www.astro.caltech.edu/GOODS_morphs/.

Some caution is required in comparing these morphological classifications over a range of redshifts. Surface brightness dimming can bias high redshift morphologies towards early-type classifications. We see evidence for this effect when we compare the 5 epoch, version-1.0 GOODS morphologies to previous determinations made by RSE for the same sample of objects in a single epoch of the version-0.5 GOODS release. The overall agreement is excellent, with the shallower single visit classes offset from the deeper stacked equivalent by only 0.1 types on the 12-class scheme defined above (see Treu et al. 2005). The standard deviation of this comparison is 1.3 morphological classes, demonstrating that the effect on the broader morphological categories, which combine three classes into one, would be minimal. Furthermore, the $z_{AB} < 22.5$ limit is one magnitude brighter than the 80% completeness limit of the ACS data for objects with half-light radii less than $1''0$ (Giavalisco et al. 2004). Thus the high signal-to-noise of the $z_{AB} < 22.5$ sample ensures robust classifications to $z \sim 1$.

Wavelength dependent morphological k -corrections are often more important for com-

parisons across different redshifts. The morphological classifications made here were carried out first in the z -band, in which the lowest redshift bin at $z \approx 0.3$ samples rest-frame R -band while the highest redshift bin at $z \approx 1$ samples rest-frame B -band. However, after the first pass, Viz color images were inspected and about 5% of the sample was corrected (by never more than one class) based on the color information. In this way, the galaxies suffering most from the morphological k -correction were accounted for.

We can gain a quantitative estimate for the remaining k -correction effect by referencing the “drift coefficients” tabulated in Table 4 of Brinchmann et al. (1998) and extrapolating them from the I -band to our z -band classifications. We would expect very small k -corrections until the highest redshift bin ($z \approx 1$) which is equivalent in wavelength to the $z = 0.7$ interval in Brinchmann et al. (1998). At this point, Brinchmann et al. (1998) estimate that $\approx 13\%$ of Spirals are misclassified as Peculiars, while the Ellipticals and Spirals exchange $\approx 25\%$ of their populations, leaving the relative numbers nearly the same.

The results of Brinchmann et al. (1998) were based on automated classifications carried out using the Asymmetry–Concentration plane, however, and may overestimate the magnitude of the k -correction. Many other groups have also investigated this effect (e.g. Kuchinski et al. 2000, 2001; Windhorst et al. 2002; Papovich et al. 2003) and suggest milder results. The k -corrections are found to be most severe when optical morphologies are compared to the mid-UV. None of the classifications in our sample were based on restframe mid-UV morphology. Furthermore, most studies have found that early-type spirals, with their mixture of star formation and evolved stellar populations, show the most drastic changes between red and UV wavelengths, while other types vary less because they are either completely dominated by young stars (late-type disks, Peculiars) or have little to no star formation at all (Ellipticals). Indeed, Conselice et al. (2005) compare visual classifications similar to those presented here in WFPC I and NICMOS H -band for 54 galaxies in HDF-N with $z < 1$ and find that only 8 disagree. Most of these were labeled as early-types in H -band and as early-type disks in I -band. Based on these various studies, we expect that the wavelength dependent k -corrections remaining in the sample are important only at the highest redshifts. Even then they are likely to be small because the z -band is still redward of the rest-frame UV. Although we choose not to explicitly correct for the morphological k -correction, we estimate that statistically over the redshift range 0.5-1, where the bulk of the evolutionary trends are seen, at most 5–10% of the populations are misidentified in our broad classification system.

2.3. Spectroscopic and Photometric Redshifts

Accurate redshifts are important not only for identifying members of a given redshift interval but for determining luminosities and stellar masses. Spectroscopic redshifts were taken from two sources. The Keck Team Redshift Survey (KTRS) provides redshifts for GOODS-N and was selected in R and carried out with DEIMOS on Keck II (Wirth et al. 2004). The KTRS is 53% complete to $R_{AB} < 24.4$, giving a sample of 1440 galaxy redshifts and providing redshifts for 761 galaxies (58%) in the GOODS-N morphological catalog described above. After our additional K_s -band requirement (see §4), this number reduces to 661 galaxies primarily because the K_s -band imaging covers only $\approx 70\%$ of GOODS-N. Spectroscopic redshifts in GOODS-S were taken from the VIMOS VLT Deep Survey (Le Fèvre et al. 2004) which is 88% complete to $I_{AB} = 24$ and accounts for 300 galaxies (25%) in the GOODS-S morphological catalog. We supplement this sample with 792 photometric redshifts (66%) from COMBO-17 (Wolf et al. 2004).

For more than half of the total morphological sample, published redshifts are not available and photometric redshifts have to be measured. In GOODS-S, 107 photometric redshifts were needed while in GOODS-N the number was 343. The inclusion of these redshifts and the requirement of K_s -band photometry yields a final morphological sample that is complete to $z_{AB} < 22.5$ and $K_s < 22.4$ (AB). We also constructed a fainter sample with $z_{AB} < 23.5$ that is too faint for reliable morphological classification but allows for investigations of completeness (see §5.2). Photometric redshifts were estimated using the Bayesian Photometric Redshift (BPZ) Code described in Benítez (2000). Using the same priors that Benítez (2000) applies to the HDF-N, we ran the BPZ software on the $1''.0$ diameter fixed-aperture ACS and K_s -band photometry, allowing for two interpolation points between templates. The KTRS and VIMOS spectroscopic redshifts were used to characterize the quality of a subset of the photometric redshifts (see Figure 1). The results were similar for both GOODS fields, with a combined mean offset of $\Delta z / (1 + z_{spec}) = -0.02$ and an rms scatter of $\sigma[\Delta z / (1 + z_{spec})] = 0.12$, similar to the precision achieved by Mobasher et al. (2004) who used BPZ to estimate redshifts in GOODS-S. We did not, however, correct for the poorer resolution ($\sim 1''.0$) of the K_s -band data.

The comparison between photo- z 's and spec- z 's in Figure 1 shows a tendency for photo- z 's to be underestimated. There is a set of objects with spec- $z < 0.5$ that have photometric redshifts near 0.2. At spec- $z \approx 1$ there is another more mild deviation toward lower photo- z 's that is likely due to the Bayesian prior (Benítez 2000) which assumes a decreasing redshift distribution at $z \sim 1$. And in general, there appears to be more catastrophic outliers with photo- z underestimates. Much of this behavior is likely related to the lack of U-band photometry, which is crucial to ruling out false low- z photometric solutions.

Over the redshift range of interest, $0.2 < z < 1.4$, the final sample consists of 1906 galaxies, of which 893 (47%) have spectroscopic redshifts and 1013 (53%) have photometric redshifts. We divide the sample into three redshift intervals, $0.2 < z < 0.51$, $0.51 < z < 0.8$, and $0.8 < z < 1.4$, chosen to balance the number of objects in each interval. The morphological breakdown (Ellipticals, Spirals, Peculiars) in each redshift bin is as follows: for $0.2 < z < 0.51$, (167, 353, 126); for $0.51 < z < 0.8$, (220, 326, 138); and for $0.8 < z < 1.4$ (131, 291, 154).

3. Determination of Stellar Masses

Estimating stellar masses using the combination of infrared imaging, multiband photometry, and redshift information is now a widely applied technique first utilized by Brinchmann & Ellis (2000). In this paper, we use a new Bayesian stellar mass code based on the precepts described in Kauffmann et al. (2003). Briefly, the code uses the multiband photometry and redshift to compare the observed SED of a sample galaxy to a grid of synthetic SEDs (from Bruzual & Charlot 2003) spanning a range of star formation histories (parameterized as an exponential), ages, metallicities, and dust content. The K -band mass-to-light ratio (M_*/L_K), stellar mass, minimum χ^2 , and the probability the model represents the data is calculated at each grid point. The probabilities are then summed across the grid and binned by stellar mass, yielding a stellar mass probability distribution for each galaxy (see Figure 2). We use the median of the distribution as an estimate of the final stellar mass. Photometry errors enter the analysis by determining how well the model SEDs can be constrained by the data. This is reflected in the stellar mass probability distribution which provides a measure of the uncertainty in the stellar mass estimate given by the width of the distribution.

In addition to accounting for photometric errors, the mass probability distribution also includes the effects of mass degeneracies in the model parameter space. These two effects typically account for 0.2 dex of uncertainty. In addition, systematic errors enter through assumptions about model parameters. In some cases, the observed SEDs do not fall in the parameter space spanned by the grid. These are characterized by large minimum χ^2 values and we add an additional 0.2 dex in quadrature to their uncertainties. The largest systematic source of uncertainty comes from our assumed IMF, in this case that proposed by Chabrier (2003). Masses derived assuming this IMF can be converted to Salpeter by adding 0.3 dex. Various tests of the stellar mass code used here under different assumptions for the IMF, the model parameter space, and the star formation parameterization are presented in Bundy et al. (2005).

Despite the large number of spectroscopic redshifts, when the stellar mass estimator is

applied to galaxies with photometric redshifts, additional errors must be included to account for the much larger redshift uncertainty. At the same time, catastrophic photo- z errors (which are apparent in Figure 1) can significantly affect mass estimates. Redshift errors enter in two ways. First, they affect the determination of the galaxy’s restframe SED because k -corrections cannot be as accurately determined. This can alter the best fitting model and the resulting mass-to-light ratio. Far more important, however, is the potential error in the luminosity distance from the increased redshift uncertainty. For the standard cosmology we have assumed, a redshift uncertainty of $\sigma[\Delta z/(1+z)] = 0.12$ can lead to an error of roughly 20% in luminosity distance. This can contribute to an added mass uncertainty of almost 50%.

The additional stellar mass uncertainty resulting from the use of photo- z ’s is illustrated in Figure 3. In this experiment, we measure photometric redshifts for galaxies that already have secure spectroscopic redshifts and use these photometric redshifts to determine a second set of stellar mass estimates. Figure 3 shows the difference in stellar mass for the same galaxies when photometric redshifts are used instead of spectroscopic redshifts, plotted as a function of their spectroscopic redshift. Individual mass estimates become less certain and there are several catastrophic outliers with stellar masses that differ by an order of magnitude. The shaded region shows the standard deviation in stellar mass error based on a Monte Carlo simulation of 20,000 galaxies in which simulated redshifts were drawn from the observed photometric redshift error distribution ($\sigma[\Delta z/(1+z)] = 0.12$). The simulation includes only the primary effect on the luminosity distance. The shaded region accounts for both the rms uncertainty and the effect of catastrophic photo- z failures since both are included in the measurement of $\sigma[\Delta z/(1+z)]$.

Figure 3 shows a systematic offset such that most of the dramatic outliers tend to have lower masses when photometric redshifts are used than when spectroscopic redshifts are used. This trend can be understood by comparing to Figure 1, which, as discussed in §2.3, shows a majority of outliers with lower photo- z measurements as compared to their spectroscopic values. The smaller luminosity distance that results from the photo- z underestimate leads to stellar masses that are also underestimated. Although we recognize this systematic trend, we do not attempt to correct for it since it primarily affects the outliers. We do add an additional 0.3 dex of uncertainty to stellar masses gleaned from the photometric redshift sample.

4. Completeness and Selection Effects in the Sample

The final sample combines several datasets leading to complicated completeness and bias effects that must be carefully examined. First, as described in §2.2, because accurate morphological classifications are required, the sample was limited to $z_{AB} < 22.5$ to ensure the fidelity of those classifications. Second, reliable stellar mass estimates at redshifts near $z \approx 1$ require three key ingredients: 1) Multi-band optical photometry, 2) K_s -band photometry, and 3) Redshifts. The optical photometry comes from the GOODS ACS imaging. Since the ACS catalog was selected in the z -band, the $z_{AB} < 22.5$ limit applies to these data as well. The K_s -band imaging was described in §2.1. As illustrated in the color-magnitude diagram in Figure 4, this depth is adequate for detecting the vast majority (95%) of the objects that lie within the area covered by the infrared imaging and satisfy the $z_{AB} < 22.5$ criterion. Thus, with the sample already limited in the z -band, requiring an additional K_s -band detection does not introduce a significant restriction and we can consider the final sample complete to $z_{AB} < 22.5$.

The third ingredient in the stellar mass estimate—the galaxy’s redshift—comes from a combination of sources (§2.3). Figure 4 plots the location on the color-magnitude diagram of those galaxies with $z_{AB} < 22.5$ that do not have spectroscopic redshifts (open symbols). They account for 54% of the final sample and are assigned redshifts based on the photo- z technique described in §2.3. The fact that almost half of the galaxies in the sample have spectroscopic redshifts is an important advantage for precise mass functions. Relying entirely on photo- z ’s would blur the edges of the redshift intervals and introduce additional uncertainty to every galaxy in the survey, as discussed in §3.

Despite the limitations of the various datasets required for this study, the final sample suffers almost exclusively from the magnitude cut in the z -band. Because it is a magnitude limited sample, it is incomplete in mass and at the highest redshifts, the objects with the reddest ($z-K_s$) colors will begin to drop out of the sample. This is illustrated by the expected location on the color-magnitude diagram of three different stellar population models, each with a luminosity of $L_K^* \approx -24$ at all redshifts (see Figure 4). Models A and B have exponential SF timescales of $\tau = 0.4$ Gyr, and metallicities of $Z=0.05$ ($2.5Z_\odot$) for A and $Z=0.02$ (Z_\odot) for B. Model C has $\tau = 4.0$ Gyr and solar metallicity. The large solid dots denote redshifts $z = 0.4, 0.8,$ and 1.2 . In the highest redshift bin ($0.8 < z < 1.4$), the redder, passively evolving sources can be expected to suffer most from the z -band cut. As these are likely to be massive, we would expect their absence to also be reflected in the combined mass function.

Following previous work (e.g. Fontana et al. 2003), we can translate the z -band cut into a conservative mass completeness limit by estimating the mass corresponding to a reasonable

maximum M_*/L_z ratio as a function of redshift. To do this, we calculate the mass of a near-instantaneous burst model with a formation redshift of $z_{form} = 10$, no dust, sub-solar metallicity, and a luminosity corresponding to an observed magnitude of $z_{AB} = 22.5$ at all redshifts. The resulting mass completeness limits rise from $10^{10} M_\odot$ at $z \sim 0.3$ to $10^{11} M_\odot$ at $z \sim 1$. In §5.3, we further discuss how mass incompleteness impacts the derived mass functions at $0.8 < z < 1.4$.

5. Results

5.1. Methods and Uncertainties

Given the small area of the GOODS fields (0.1 square degrees), cosmic variance and clustering in these intervals will affect the mass functions we derive. Somerville et al. (2004) present a convenient way to estimate cosmic variance based on the number density of a given population and the volume sampled. Using these techniques, we estimate that uncertainties from cosmic variance range from $\approx 20\%$ in the highest redshift bin to $\approx 60\%$ in the lowest. This translates into an additional 0.1–0.3 dex of uncertainty in the final mass functions.

In deriving a mass or luminosity function in a magnitude limited survey, faint galaxies not detected throughout the entire survey volume must be accounted for. Many techniques exist to accomplish this while preventing density inhomogeneities from biasing the shape of the derived luminosity function (for a review, see Willmer 1997). However, there is no cure for variations from clustering and cosmic variance. With an expected uncertainty from cosmic variance of $\sim 40\%$ on average, these variations will affect comparisons we might draw between redshift intervals. Given these limitations we adopt the simpler V_{max} formalism (Schmidt 1968). The V_{max} estimate is the volume corresponding to the highest redshift, z_{max} , at which a given galaxy would still appear brighter than the $z_{AB} = 22.5$ magnitude limit and would remain in the sample. For a galaxy i in a redshift interval, $z_{low} < z < z_{hi}$,

$$V_{max}^i = d\Omega \int_{z_{low}}^{\min(z_{hi}, z_{max})} \frac{dV}{dz} dz \quad (1)$$

where $d\Omega$ is the solid angle subtended by the survey and dV/dz is the comoving volume element.

The stellar mass estimator fits a model spectrum to each galaxy. By redshifting this model spectrum and integrating it over the z -band filter response function, we can calculate the apparent z -band magnitude as a function of redshift, implicitly accounting for

the k -correction. The quantity, z_{max} , is determined by the redshift at which the apparent magnitude becomes fainter than $z_{AB} = 22.5$.

Once V_{max} is estimated, we calculate the comoving number density of galaxies in a particular redshift bin and stellar mass interval, $(M_* + dM_*)$, as,

$$\Phi(M_*)dM_* = \sum_i \frac{1}{V_{max}^i} dM_* \quad (2)$$

where the sum is taken over all galaxies i in the interval.

The V_{max} formalism is appealing because it is easy to apply and makes no assumptions on the form of the luminosity or mass function. It can be biased by clustering since it assumes galaxies are uniformly distributed through the survey volume. This bias is best understood through the observed redshift distributions (Figure 5). In the lowest redshift bin, the concentration at the high end of the redshift interval near $z = 0.47$ leads to an underestimate in the mass function, especially for the number densities of fainter galaxies that cannot be detected at the furthest distances in this interval. In the highest redshift bin, the redshift spikes at the low- z end have the opposite effect. In this case, the clustering increases the resulting mass function by causing an overestimate of galaxies that would not be detected if the redshift distribution was more uniform. Clustering can also affect the type-dependent stellar mass functions because early-type galaxies are expected to be more strongly clustered than later types.

Other uncertainties in deriving the mass function are greatly reduced by utilizing spectroscopic redshifts. The effect on the mass functions caused by uncertainty in photo- z estimates and stellar mass errors is estimated in the following way. We use a Monte Carlo technique to simulate 100 realizations of our dataset, utilizing the resulting variation in the observed mass functions to interpret the errors. For a given realization, the stellar mass of each galaxy is drawn randomly from the stellar mass probability distribution determined by the mass estimator (see §3); thus avoiding any assumption about the form of the estimated mass distribution. Galaxies with photometric redshifts tend to smear out the edges of the redshift intervals. In the simulations, the realized redshift for these galaxies is drawn from a Gaussian distribution with $\sigma = \sigma[\Delta z / (1 + z_{spec})] = 0.12$, the same rms measured for galaxies with both spectroscopic and photometric redshifts. The effect of this redshift uncertainty on the luminosity distance is also included in the stellar mass error budget (see §3).

5.2. Galaxy Stellar Mass Functions

We plot the resulting galaxy stellar mass functions for all types in Figure 6. The solid lines trace the best fit to the local mass function measured by Cole et al. (2001) (we do not plot the results of Bell et al. (2003) which are consistent with Cole et al. (2001)). The redshift dependent mass functions derived by Drory et al. (2004) (also plotted as “plus” symbols) come from a larger photo- z sample that is most complete at higher masses. Results from the spectroscopic K20 survey are shown as squares (Fontana et al. 2004). We note that the lower result from Fontana et al. (2004) in the high- z bin may be caused by mismatched redshift intervals. Their result for $1.0 < z < 1.5$ is plotted, but their $0.7 < z < 1.0$ mass function (shown in the middle plot of Figure 6) may provide a more adequate comparison considering our high- z bin includes many galaxies in the range, $0.8 < z < 1.0$.

Also plotted in Figure 6 are the combined mass functions for a larger, unclassified, photometric sample where the z -band magnitude cut has been increased to $z_{AB} = 23.5$. Though reliable visual morphological classification is not feasible for objects in the ACS data with $z_{AB} > 22.5$, the fainter sample demonstrates the effects of incompleteness in the primary ($z_{AB} = 22.5$) catalog, which become particularly important in the highest redshift bin. The point at which the morphological sample begins to show a deficit with respect to the fainter sample is consistent with the mass completeness limits calculated based on the maximum M_*/L_z ratio (see §4). For the three redshift intervals, the estimated mass incompleteness limits are, in order of increasing redshift, $10^{10} M_\odot$, $4 \times 10^{10} M_\odot$, and $10^{11} M_\odot$. As discussed in §5.1, in addition to completeness, cosmic variance and clustering dominate the small GOODS area and make interpretations of the mass function difficult.

We fit Schechter functions to the binned data, including fits to separate morphological populations (see §5.3), and show the resulting parameters in Table 1. The primary and extended samples are quite similar in the first two redshift intervals, with incompleteness in the primary sample becoming significant in the third ($0.8 < z < 1.4$). Across the full redshift range, the combined mass function shows little evolution and remains similar in shape to its form at $z = 0$.

These results are consistent with previous work. Fontana et al. (2004) find little evolution out to $z \sim 1$ in the mass function derived from the K20 survey (also plotted). The K20 sample (Cimatti et al. 2002) has good spectroscopic coverage (92%) but is slightly shallower (0.5 mag in K) and roughly one quarter of the size of the sample studied here. The MUNICS survey (Drory et al. 2001), in contrast, contains 5000 galaxies spread over several fields, covering a much larger area. It is roughly one and a half magnitudes shallower in K and consists primarily ($\approx 90\%$) of photometric redshifts. Drory et al. (2004) argue that the MUNICS combined mass function exhibits significant evolution to $z = 1.2$, with a decrease in

the characteristic mass and steepening of the faint-end slope. Considering the uncertainties, we feel the MUNICS result is consistent with the work presented here although we differ in the interpretation.

Theoretical models currently yield a variety of predictions for the combined galaxy stellar mass functions. Fontana et al. (2004) compare predictions from several groups with various techniques including semi-analytic modeling and numerical simulations. In general, semi-analytic models (e.g. Cole et al. 2000; Somerville et al. 2001; Menci et al. 2004) tend to produce mass functions that evolve strongly with redshift, with decreasing normalization and characteristic masses that together underpredict the observed number of massive, evolved galaxies at high redshift. Rapid progress in addressing this problem is currently underway. Numerical models (e.g. Nagamine et al. 2004) better reproduce a mildly evolving mass function and more easily account for high mass galaxies at $z \sim 1$, but sometimes overpredict their abundance (see the discussion in §5.3 on massive galaxies). Observations of the galaxy stellar mass function and its evolution thus provide key constraints on these models.

5.3. Type-Dependent Galaxy Mass Functions

In Figure 7, we show the galaxy stellar mass functions for the three broad morphological populations derived using the V_{max} formalism described in §5.1. As a check, we also calculated mass functions after applying a z -band absolute magnitude limit of $M_z < -20.3$, to which nearly every galaxy can be detected at every redshift. Absolute magnitudes are determined through SED fitting as part of the stellar mass estimator (§5.1). Though less complete, the general characteristics of the mass functions with $M_z < -20.3$ agree well at high stellar masses with those derived using the V_{max} method.

All three redshift bins in Figure 7 are complete at $M_* > 10^{11} M_\odot$, and little difference is seen in the combined mass function between the morphological sample (with $z_{AB} < 22.5$) and the fainter sample ($z_{AB} < 23.5$). This allows for a comparison of the morphological makeup of the high-mass population. In the highest redshift bin, we find that Spirals are slightly favored at $M_* \approx 10^{11} M_\odot$ and are competitive with E/S0's at $M_* \approx 3 \times 10^{11} M_\odot$. At the same time, Peculiars make a significant contribution at these masses. Both the Peculiar and Spiral populations drop at lower redshifts as E/S0's become increasingly dominant at high masses.

Turning now to the broader range of masses sampled by the data, the first redshift bin exhibits a transitional mass of $M_{tr} \approx 2-3 \times 10^{10} M_\odot$ ($\log_{10} M_{tr} \approx 10.3-10.5$) below which the E/S0 population declines while the Spiral population rises, becoming the dominant

contributor to the combined mass function. Across the three redshift bins studied here, it appears this transitional mass shifts to lower mass with time as the contribution of the E/S0 population to low mass galaxies increases. We caution that M_{tr} is close to the estimated mass completeness limit, especially in the $0.55 < z < 0.8$ redshift bin.

Tracing evolution at masses below M_{tr} is difficult because of incompleteness. As discussed in §4, we would expect early-type galaxies to be increasingly absent in the z -selected sample at higher redshifts. Thus, much of the more rapid decline in the E/S0 contribution at $0.8 < z < 1.4$ may be due to the z -band magnitude cut. When our cut is relaxed to $z_{AB} = 23.5$, we can expect that many of these missing E/S0's will re-enter the sample and that this would drive the combined mass function to levels more comparable to those observed at lower redshift. One line of evidence in support of this is the predominantly red ($V - K_s$) color of the galaxies introduced into the sample when the z_{AB} limit is relaxed to 23.5. For stellar masses greater than $\approx 10^{10} M_{\odot}$, the ($V - K_s$) distribution of these galaxies is very similar to the E/S0 population in the $z_{AB} < 22.5$ sample. Their low asymmetries, as measured through the CAS system (Conselice 2003), are also consistent with an E/S0 population. With decreasing stellar mass, the asymmetry values increase and the color distribution spreads towards the blue, suggesting that, at lower masses, other galaxy types enter the fainter, high- z sample as well.

Our suggestion that an E/S0 population is primarily responsible for adjusting the combined mass function (for $M_* \gtrsim 10^{10} M_{\odot}$) is also consistent with the contribution of Spirals which, in the high- z bin, is a factor of $\sim 70\%$ lower at $M_* = 1.6 \times 10^{10} M_{\odot}$ ($\log_{10} M_*/M_{\odot} = 10.2$) than in the mid- z bin. At this same mass in the high- z bin, however, the combined mass function increased by almost an order of magnitude when galaxies with $z_{AB} < 23.5$ are included. Much of this increase is likely to come from E/S0's that were previously missed.

5.4. Integrated Stellar Mass Density

Following Brinchmann & Ellis (2000), in Figure 8 we show results for the type-dependent stellar mass density as a function of redshift. In this analysis we have implemented a mass limit of $M_* > 10^{11} M_{\odot}$, thus we are mass complete in all three redshift bins. We find that the total stellar mass density grows by $\simeq 30\%$ from $z \sim 1$ to $z = 0$, although the uncertainty from cosmic variance is large. The morphological breakdown of the increase in stellar mass density illustrates a demise in the contribution from Spirals and Peculiars accompanied by a rise in the density of Ellipticals. The error bars indicated on Figure 8 were calculated using the same Monte Carlo technique that was applied to the mass functions. In this way, the uncertainties account for errors in photometry, stellar mass estimates, and photometric

redshifts. The shaded region in Figure 8 demonstrates the expected uncertainty due to cosmic variance.

The observed 30% increase in the integrated stellar mass density is consistent with measurements by other groups (e.g. Cohen 2002; Fontana et al. 2003; Dickinson et al. 2003) and can be reconciled with the observed star formation rate over the same redshift range (e.g. Fontana et al. 2003). As shown in Figure 8, we find similar results for the morphological dependence of the growth of stellar mass as Brinchmann & Ellis (2000). The sample presented here is more complete because it was selected in z -band not I -band and is almost 7 times larger, resulting in smaller random errors. We note that Brinchmann & Ellis (2000) do not estimate the affect of cosmic variance on their sample, which we find to be the primary uncertainty, nor do they ensure their sample is mass complete. As suggested by Brinchmann & Ellis (2000), the rise of the Elliptical population implies that other galaxies, including Peculiar and Spirals, transform into early-type galaxies with time.

6. Discussion

In broad terms, our results support two independent and consistent perspectives on the mass assembly history of galaxies since $z \sim 1$. On the one hand, global measures of the mass distribution, such as the combined galaxy stellar mass function, show little evolution in the distribution of massive galaxies from $z \sim 1$ to $z = 0$. This implies that much of the observed star formation and associated stellar growth over this interval occurs in lower mass galaxies. On the other hand, a more dynamic perspective emerges when the mass distribution is considered according to galaxy type. In this paper, we have shown that although the number density of massive galaxies is relatively fixed after $z \sim 1$, the morphological composition of this population is still changing, such that the more balanced mix of morphological types at $z \sim 1$ becomes dominated by ellipticals at the lowest redshifts. Strikingly, this morphological evolution also appears to occur first at the highest masses, proceeding to rearrange the morphologies of lower mass galaxies as time goes on. In this section, we explore how these two perspectives—little total stellar mass evolution overall accompanied by more substantial internal changes—lend insight into the mechanisms responsible for the growth of galaxies and the development of the Hubble Sequence.

As we discuss in §5.2, the observed stellar mass function, which is not affected by incompleteness at high mass in our survey, shows little evolution from $z \sim 1$ to $z = 0$ in agreement with previous work (e.g. Drory et al. 2004; Fontana et al. 2004; Bell et al. 2004). Although it appears that the stellar content of massive galaxies is relatively well established by $z \sim 1$, the nature of these galaxies continues to change. This effect can be seen in

Figure 7 in the mass bin centered at $10^{11} M_{\odot}$ ($10.8 < \log M_*/M_{\odot} < 11.2$) where, in all three redshift intervals, our sample is complete with respect to a maximum M_*/L_K ratio. Ellipticals, Spirals, and Peculiars contribute in similar numbers at the highest redshift, while at the lowest redshift, Ellipticals clearly dominate. This trend is similar to the growth in stellar mass density of these morphological populations as observed by Brinchmann & Ellis (2000) and illustrated in Figure 8.

Studying this growth as a function of mass provides additional information on how Ellipticals come to dominate the massive galaxy population by $z \sim 0.3$. This growth of Ellipticals could arise from several processes including the formation of completely new galaxies, stellar mass accretion onto established systems of smaller mass, and the transformation of other established galaxies into ones with early-type morphologies. It is likely that all three processes contribute at some level, although the fact that the density of high-mass galaxies changes little since $z \sim 1$ places an important constraint on the amount of new growth, either through star formation or the build-up of smaller galaxies, that is possible. This growth is limited to at most a factor of ~ 2 while the density of Ellipticals at $M_* \approx 10^{11} M_{\odot}$ increases by a factor of ~ 3 . A more detailed examination of the effect of stellar mass accretion onto lower mass Ellipticals is difficult because of incompleteness in our survey. We estimate, however, that the typical stellar mass of an Elliptical with $M_* \approx 3 \times 10^{10} M_{\odot}$ would have to at least triple in order to contribute significantly to the increasing proportion of high-mass Ellipticals. This spectacular growth in a just a few Gyr seems unlikely. Finally, Figure 7 shows that the rise of massive Ellipticals is accompanied by a *decline* in the other two populations. Thus, assuming that galaxies cannot be broken up or destroyed, morphological transformation of individual galaxies, whether through merging or some other mechanism like disk fading, must be a significant driver in the evolution toward early-type morphologies.

At $z \sim 1$, the higher number of massive Peculiars—often associated with interacting systems—is suggestive that at least some of this morphological transformation is occurring through mergers, which are known to be more frequent at high- z (e.g Le Fèvre et al. 2000; Conselice et al. 2003). Indeed, Hammer et al. (2004) emphasize the importance of luminous IR galaxies (LIRGs), thought to be starbursts resulting from merging at these masses. And Bundy et al. (2004), examined galaxies with a broader range of stellar mass, and used observations of the IR pair fraction to estimate that the total stellar mass accreted through merging since $z \sim 1$ is approximately $\Delta\rho_*^m \sim 10^8 M_{\odot}\text{Mpc}^{-3}$. As illustrated in Figure 8, this is close to the magnitude of the observed growth in the mass density of Ellipticals ($\Delta\rho_* \sim 8 \times 10^7 M_{\odot}\text{Mpc}^{-3}$), implying that merging may have an impact on the morphological transformation occurring among massive galaxies.

Turning now to the full range of stellar mass accessible in our sample, one of the key

results of this work is the observation of a transitional mass, M_{tr} , above which Ellipticals dominate the mass function and below which Spirals dominate. This phenomenon is observed in studies at low redshift. Bell et al. (2003) find a cross-over point at $M_{tr} \approx 3 \times 10^{10} M_{\odot}$ between the local stellar mass functions of early and late type galaxies, as classified by the concentration index (see the g -band derived stellar mass functions in their Figure 17). Analysis of the Sloan Digital Sky Survey (SDSS) reveals a similar value for M_{tr} (Kauffmann et al. 2003; Baldry et al. 2004) which also serves as the dividing line in stellar mass for a number of bimodal galaxy properties separating early from late types. These include spectral age diagnostics (like $D_n(4000)$ and $H\delta_A$), surface mass densities, size and concentration, and the frequency of recent star bursts.

Theoretical work by Dekel (2004) suggests that, in addition to mergers, the effects of shock heating and supernova (SN) feedback weigh heavily on the evolution of galaxies, and both set characteristic scales that correspond to a stellar mass of $3 \times 10^{10} M_{\odot}$ today. Galaxies form in halos below the M_{shock} threshold. If they remain below the SN feedback threshold, then SN feedback regulates star formation, leading to young, blue populations and a series of well defined scaling relations. Galaxies with masses above M_{shock} are formed by the merging of progenitors. Their gas is shock heated and may be prevented from cooling by AGN feedback, leading to older, redder populations and a different set of scaling laws (see Birnboim & Dekel 2003). The SN characteristic scale is expected to decrease with redshift while the shock heating scale remains constant (Dekel, private communication), so it is unclear how these physical scales are related to the evolution of M_{tr} for $z \lesssim 1$.

Whatever the processes at work, the interplay of the morphological populations and the possible evolution in M_{tr} as traced by Figure 7 seem to echo patterns in the global star formation rate as observed at higher redshift; the most morphologically evolved galaxies appear first at the highest masses, and their dominance over other populations spreads toward lower masses—thereby reducing M_{tr} —as time goes on. This is similar to the concept of “downsizing” (Cowie et al. 1996) in which the highest mass galaxies stop forming stars at the earliest times while progressively less massive galaxies end their star formation later. Although the evolution of star formation and morphology both appear to proceed first at the highest masses, downsizing as it relates to star formation predates morphological transformation by at least 1–2 Gyr. As reported by Juneau et al. (2004), the SFR of high-mass galaxies ($M_* > 6 \times 10^{10} M_{\odot}$) goes through a transition at $z \approx 1.5$, emerging from a “burst phase” (in which the SFR multiplied by the age of the universe becomes comparable to the stellar mass) to become quiescent. According to Figure 7, these same high-mass galaxies are still evolving morphologically at $z \approx 0.8$, more than 1 Gyr later. This implies that the timescale of the transformation process is ~ 1 Gyr, similar to the merger timescale, which is often estimated at 0.5 Gyr (e.g. Patton et al. 2000).

Downsizing may apply not only to galaxies undergoing bursts of vigorous star formation on short timescales but also to relatively quiescent galaxies with continuing, modest star formation. Treu et al. (2004), for example, find that while massive spheroidals have mostly completed their star formation by $z \sim 2$, low mass field ellipticals exhibit continuing star formation from $z < 1$. Thus, the pattern of downsizing in both star formation and morphology is gradual and appears to operate over a large range in mass and extend to the lowest redshifts.

The growing evidence for downsizing and its morphological extension raises many questions. While mergers offer a natural explanation for the link between the continuing star formation and morphological transformations we present in this paper, it is not clear what is driving this mass-dependent downsizing behavior. Most likely several competing physical processes, including mass-dependent galaxy mergers, are responsible for shaping the Hubble Sequence.

7. Summary

We have studied the redshift dependent mass functions for three distinct morphological populations in a sample of 2150 galaxies with $z_{AB} < 22.5$ in the GOODS fields. For 44% of the sample, spectroscopic redshifts from the KTRS and VLT VIMOS surveys are available. We use photometric redshifts from the COMBO17 survey in GOODS-S for 37% of the sample and estimate photometric redshifts based on $BViz$ ACS photometry for the remaining 19%. We utilize K_s -band observations of GOODS-N taken with the WIRC camera at Palomar Observatory and public K_s -band imaging of GOODS-S from the EIS survey to estimate stellar masses for the whole sample based on fitted mass-to-light ratios.

We find very little evolution in the shape of the combined mass function, which we fit using Schechter functions with slope, $\alpha \approx -1.2$ and $\log_{10} M^* h^2 \approx 10.8\text{--}11.0$ over the whole redshift range studied ($0.2 < z < 1.4$). This is consistent with Fontana et al. (2004) and appears similar to Drory et al. (2004) though Drory et al. (2004) interpret their results as evidence for stronger evolution. Cosmic variance resulting from the small size of the GOODS fields is our primary source of uncertainty. The lack of significant evolution in the observed mass function implies that much of the stellar growth occurring since $z \sim 1$ takes place at lower masses not yet accessible to high- z stellar mass surveys.

Our main result is the type-dependent galaxy stellar mass functions over three redshift intervals spanning the range, $0.2 < z < 1.4$. The morphological breakdown of the most massive galaxies ($M_* \approx 10^{11} M_\odot$) changes significantly with redshift. At $z \sim 1$, Ellipti-

icals, Spirals, and Peculiars are present in similar numbers. By a redshift of 0.3, Ellipticals dominate the high-mass population, suggesting that merging or some other transformation process is active.

At all redshifts in our sample, Spirals and Peculiars dominate at lower masses while E/S0’s become prominent at higher masses. The observed transition mass, $M_{tr} = 2\text{--}3 \times 10^{10} M_{\odot}$, is similar to that apparent in lower redshift studies. There is evidence that M_{tr} was higher at early times, suggesting a morphological extension of the “downsizing” pattern observed in the star formation rate. Just as the most massive galaxies emerge from a phase of rapid star formation at the earliest times, massive galaxies are also the first to evolve into predominantly early-type morphologies. This morphological transformation is completed 1–2 Gyr after the galaxies leave their bursting phase.

Finally, we derive the integrated stellar mass densities of the three populations and find similar results as Brinchmann & Ellis (2000). We find further evidence for the transformation of Peculiars as well as Spirals into early-type galaxies as a function of time. Based on the observed mass functions, this transformation process appears to be more important at lower masses ($M_* \lesssim 10^{11} M_{\odot}$) because the most massive E/S0’s are already in place at $z \sim 1$.

In the future it will be possible to extend this kind of study with the primary aim of reducing statistical uncertainty and the effects of cosmic variance. Large galaxy surveys like DEEP2 (Davis et al. 2002) and COMBO-17 (Rix et al. 2004) are promising in this regard because they contain tens of thousands of galaxies spread over a wide area, although we note that stellar mass studies benefit greatly from spectroscopic redshifts. Extending the combined mass function to lower masses may help reveal the nature of star formation from $z \sim 1$ to $z = 0$. At the same time, reducing cosmic variance will allow for more detailed studies on the type-dependent evolution of the mass function and its relation to merging and star formation.

We wish to thank the referee for very valuable comments, Tommaso Treu for help developing the morphological classification scheme and for useful discussions, and Jarle Brinchmann for advice on the stellar mass estimator. We also thank Avishai Dekel for helpful discussions.

Supported by NSF grant AST-0307859 and NASA STScI grant HST-AR-09920.01-A.

REFERENCES

- Abraham R. G., van den Bergh, S., Glazebrook, K., Ellis, R. S., Santiago, B. X., Surma, P., & Griffiths, R. E. 1996, *ApJS*, 107, 1
- Baldry, I. K., Glazebrook, K., Brinkmann, J., Ivezić, Ž., & Szalay, A. S. 2004, *ApJ*, 600, 681
- Baugh, C. M., Benson, A. J., Cole, S., Frenk, C. S., & Lacey, C. 2002, astro-ph/0203051
- Baugh, C. M., Cole, S., Frenck, C. S., & Lacey, C. G. 1998, *ApJ*, 498, 504
- Bell, E. F., McIntosh, D. H., Katz, N., & Weinberg, M. D. 2003, *ApJS*, 149, 289
- Bell, E. F. et al. 2004, *ApJ*, 608, 752
- Benítez, N. 2000, *ApJ*, 536, 571
- Bertin, E. & Arnouts, S. 1996, *A&A*, 117, 393
- Birnboim, Y. & Dekel, A. 2003, *MNRAS*, 345, 349
- Blain, A. W., Smail, I., Ivison, R. J. & Kneib, J.-P. 1999, *MNRAS*, 302, 632
- Bouwens, R. J., et al. 2003, *ApJ*, 595, 589
- Brinchmann, J. & Ellis, R. S. 2000, *ApJ*, 546, L77
- Brinchmann, J., et al. 1998, *ApJ*, 499, 112
- Bruzual, G., & Charlot, S. 2003, *MNRAS*, 344, 1000B
- Bundy, K., Fukugita, M., Ellis, R. S., Kodama, T., & Conselice, C. J. 2004, *ApJ*, 601, 123
- Bundy, K. et al. 2005, in prep.
- Bunker, A. J., Stanway, E. R., Ellis, R. S., & McMahon, R. G. 2004, astro-ph/0403223
- Chabrier, G. 2003, *PASP*, 115, 763
- Chapman, S. C., Blain, A. W., Ivison, R. J., & Smail, I. R. 2003, *Nature*, 422, 695
- Cimatti A., et al. 2002, *A&A*, 392, 395
- Cohen, J. G. 2002, *ApJ*, 567, 672
- Cole, S., Lacey, C. G., Baugh, C. M., & Frenk, C. S. 2000, *MNRAS*, 319, 168

- Cole, S., et al. 2001, MNRAS, 326, 255
- Conselice, C. J. 2003, ApJS, 147, 1
- Conselice, C. J., Bershad, M. A., Dickinson, M., & Papovich, C. 2003, AJ, 126, 1183
- Conselice, C. J. et al. 2005, ApJ, in press, astro-ph/0405001
- Cowie, L. L., Songalia A., Hu, E. M., & Cohen, J. G. 1996, AJ, 112, 839
- Davis, M., et al. 2002, SPIE, 4834, 161
- Dekel, A. 2004, astro-ph/0401503
- Dickinson, M., Papovich, C., Ferguson, H., & Budavári, T. 2003, ApJ, 587, 25
- Drory, N., Bender, R., Feulner, G., Hopp, U., Maraston, C., Snigula, J., & Hill, G. J. 2004, astro-ph/0403041
- Drory, N., Feulner, G., Bender, R., Botzler, C. S., Hopp, U., Maraston, C., Mendes de Oliveira, C., & Snigula, J. 2001, MNRAS, 325, 550
- Ellis, R. S., Colless, M., Broadhurst, T., Heyl, J., & Glazebrook, K. 1996, MNRAS, 280, 235
- Fall, S. M., Charlot, S., & Pei, Y. C. 1996, ApJ, 464, 43
- Feulner G., Goranova, Y., Drory, N., Hopp, U., & Bender, R. 2004, MNRAS, submitted, astro-ph/0411774
- Fontana, A., et al. 2003, ApJ, 594, L9
- Fontana, A., et al. 2004, astro-ph/0405055
- Franceschini, A., Silva, L., Fasano, G., Granato, G. L., Bressan, A., Arnouts, S., & Luigi, D. 1998, ApJ, 506, 600
- Fukugita, M., Hogan, C. J., & Peebles, P. J. E. 1998, ApJ, 503, 518
- Giavalisco, M., et al. 2004, ApJ, 600, L93
- Glazebrook, K., Ellis, R. S., Santiago, B., & Griffiths, R. 1995, MNRAS, 275, 19
- Hammer, F., Flores, H., Elbaz, D., Zheng, X. Z., Liang, Y. C., & Cesarsky, C. 2004, A&A, submitted, astro-ph/0410518
- Juneau, S. et al. 2004, ApJ, submitted, astro-ph/0411775

- Kauffmann, G., et al. 2003, MNRAS, 341, 33
- Kauffmann, G., et al. 2003, MNRAS, 341, 54
- Kuchinski, L. E. et al. 2000, ApJS, 131, 441
- Kuchinski, L. E., Madore, B. F., Freedman, W. L., & Trewhella, M. 2001, AJ, 122, 729
- Le Fèvre, O. et al. 2004, astro-ph/0409133
- Le Fèvre, O., et al. 2000, MNRAS, 311, 565
- Lilly, S. J., Le Fèvre, O., Crampton, D., Hammer, F., & Tresse, L., 1995, ApJ, 455, 50
- Lilly, S. J., Le Fèvre, O., Hammer, & F., & Crampton, D., 1996, ApJ, 460, L1
- Madau, P., Ferguson, H. C., Dickinson, M. E., Giavalisco, M., Steidel, C. C., & Fruchter, A. 1996, MNRAS, 283, 1388
- Menci, N., Cavaliere, A., Fontana, A., Giallongo, E., Poli, F., & Vittorini, V. 2004, ApJ, 604, 12
- Mobasher, B., et al. 2004, ApJ, 600, L167
- Nagamine, K., Cen, R., Hernquist, L., Ostriker, J. P., & Springel, V. 2004, astro-ph/0311294
- Papovich, C., Giavalisco, M., Dickinson, M., Conselice, C. J., & Ferguson, H. C. 2003, ApJ, 598, 827
- Patton, D. R., Carlberg, R. G., Marzke, R. O., Pritchett, C. J., da Costa, L. N., & Pellegrini, P. S. 2000, ApJ, 536, 153
- Rix, H.-W. et al. 2004, ApJS, 152, 163
- Rudnick, G., et al. 2003, ApJ, 599, 847
- Saracco, M. et al. 2004, MNRAS, submitted, astro-ph/0412020
- Schmidt, M. 1968, ApJ, 151, 393
- Shapley, A.E., Steidel, C.C., Pettini, M., Adelberger, K.L. 2003, ApJ, 588, 65
- Somerville, R. S. 2004, astro-ph/0401570
- Somerville, R. S., Lee, K., Ferguson, H. C., Garner, J. P., Moustakas, L. A., & Giavalisco, M. 2004, ApJ, 600L, 171S

- Somerville, R. S., Primack, J. R., & Faber, S. M. 2001, MNRAS, 320, 504
- Steidel, C. C., Adelberger, K. L., Giavalisco, M., Dickinson, M., & Pettini, M. 1999, ApJ, 519, 1S
- Sullivan, M., Treyer, M. A., Ellis, R. S., & Bahram, M. 2004, MNRAS, 350, 21
- Treu, T., Ellis, R. S., Liao, T. X., & van Dokkum, P. G. 2004, ApJ, submitted
- Treu, T. et al. 2004, ApJ, in prep
- Vandame, B. et al. 2001, A&A, submitted, astro-ph/0102300
- Willmer, C. N. A. 1997, AJ, 114, 3
- Wilson, J. C., et al. 2003, SPIE, 4851, 451
- Windhorst, R. A. et al. 2002, ApJS, 143, 113
- Wirth, G. D., et al. 2004, AJ, in press
- Wolf, C., et al. 2004, A&A, 421, 913

Table 1. Stellar Mass Function Parameters

Sample	Total			GOODS-N			GOODS-S		
	ϕ^*	α	$\log_{10} M^* h^2$	ϕ^*	α	$\log_{10} M^* h^2$	ϕ^*	α	$\log_{10} M^* h^2$
$0.2 < z < 0.55$									
All	5.4 ± 0.9	-1.04 ± 0.18	10.85 ± 0.10	5.8 ± 1.3	-1.03 ± 0.21	10.81 ± 0.10	4.9 ± 0.5	-1.05 ± 0.11	10.86 ± 0.06
All $z_{AB} < 23.5$	4.3 ± 0.7	-1.16 ± 0.16	10.94 ± 0.08	4.0 ± 0.5	-1.18 ± 0.11	10.99 ± 0.06	4.1 ± 1.2	-1.16 ± 0.27	10.92 ± 0.13
E/S0	4.5 ± 1.5	-0.42 ± 0.48	10.70 ± 0.15	3.8 ± 0.5	-0.56 ± 0.15	10.74 ± 0.06	5.6 ± 1.1	-0.16 ± 0.47	10.52 ± 0.09
Spiral	3.4 ± 0.7	-1.08 ± 0.25	10.58 ± 0.11	3.1 ± 0.5	-1.15 ± 0.16	10.69 ± 0.09	1.1 ± 0.1	-1.35 ± 0.06	10.90 ± 0.06
Peculiar	0.1 ± 0.0	-1.60 ± 0.12	11.52 ± 0.24	0.1 ± 0.0	-1.51 ± 0.06	11.45 ± 0.16	0.3 ± 0.0	-1.60 ± 0.13	10.71 ± 0.10
$0.55 < z < 0.8$									
All	11.9 ± 1.5	-0.51 ± 0.33	10.67 ± 0.05	10.0 ± 1.0	-0.45 ± 0.26	10.65 ± 0.04	15.3 ± 1.1	-0.48 ± 0.20	10.70 ± 0.03
All $z_{AB} < 23.5$	8.6 ± 1.5	-1.09 ± 0.39	10.83 ± 0.06	6.2 ± 1.1	-1.15 ± 0.22	10.86 ± 0.07	9.6 ± 1.8	-1.18 ± 0.30	10.91 ± 0.06
E/S0	6.0 ± 0.4	0.22 ± 0.22	10.55 ± 0.02	4.4 ± 0.5	0.26 ± 0.45	10.52 ± 0.05	8.0 ± 0.6	0.00 ± 0.22	10.68 ± 0.03
Spiral	5.0 ± 2.3	-0.69 ± 1.04	10.66 ± 0.19	4.6 ± 0.7	-0.68 ± 0.37	10.66 ± 0.07	6.0 ± 0.7	-0.57 ± 0.40	10.62 ± 0.05
Peculiar	1.5 ± 1.3	-1.01 ± 1.19	10.55 ± 0.31	0.7 ± 0.2	-0.81 ± 0.29	11.18 ± 0.53	1.4 ± 0.5	-1.03 ± 0.31	11.03 ± 0.36
$0.8 < z < 1.4$									
All	5.3 ± 0.5	-0.50 ± 0.36	10.80 ± 0.03	6.8 ± 0.3	-0.02 ± 0.16	10.72 ± 0.01	3.1 ± 0.3	-0.88 ± 0.33	10.84 ± 0.03
All $z_{AB} < 23.5$	6.2 ± 5.4	-1.19 ± 2.66	10.90 ± 0.28	9.1 ± 1.2	-0.99 ± 0.30	10.86 ± 0.02	3.5 ± 0.8	-1.50 ± 0.34	10.92 ± 0.06
E/S0	1.5 ± 0.2	0.11 ± 0.45	10.73 ± 0.04	1.8 ± 0.1	0.64 ± 0.23	10.62 ± 0.02	1.2 ± 0.3	-0.61 ± 0.64	10.83 ± 0.11
Spiral	3.1 ± 0.4	-0.24 ± 0.46	10.73 ± 0.04	4.0 ± 0.5	-0.14 ± 0.42	10.74 ± 0.05	1.1 ± 0.3	-0.75 ± 0.66	11.02 ± 0.17
Peculiar	0.7 ± 0.4	-1.23 ± 0.72	10.92 ± 0.21	0.6 ± 0.2	-0.52 ± 0.76	10.90 ± 0.14	1.4 ± 0.4	-0.74 ± 0.55	10.60 ± 0.07

Fig. 1.— Results of the photometric redshift estimation using the BPZ code by Benítez (2000). The plot illustrates the difference between photo-z's and spectroscopic redshifts (where they exist).

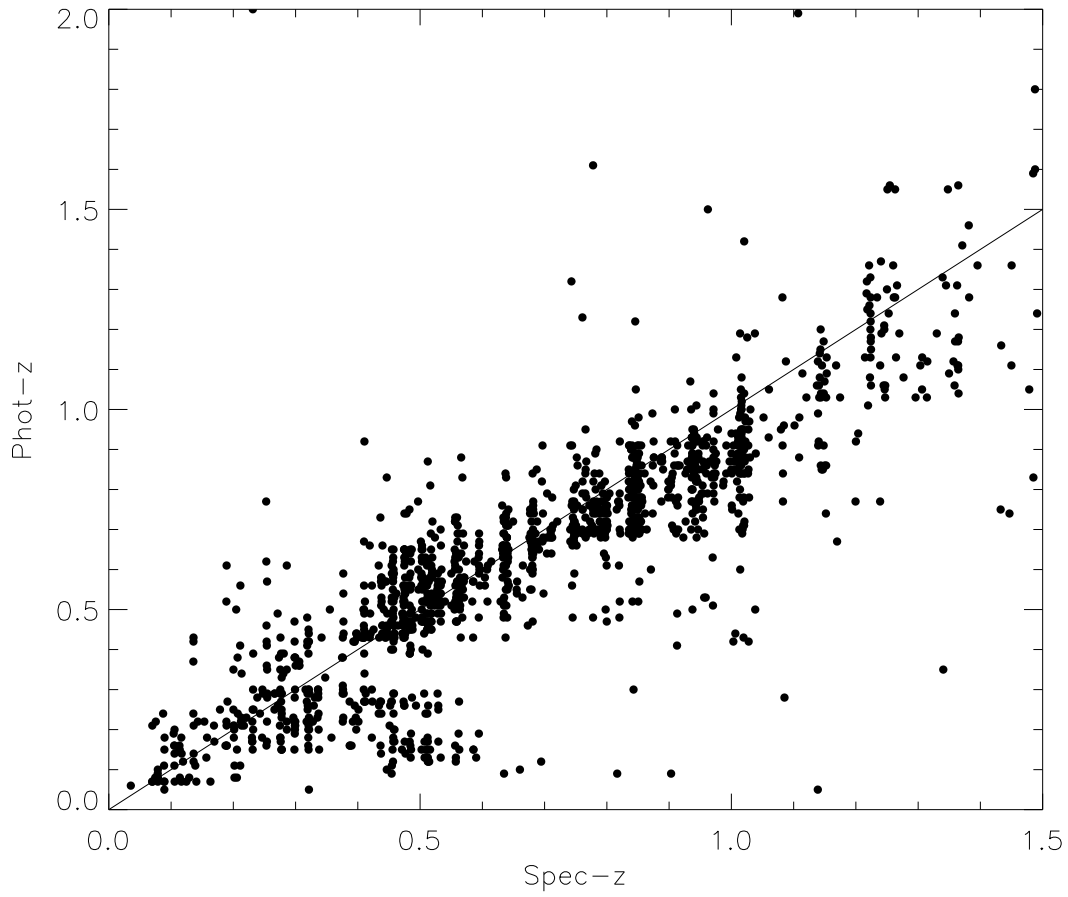


Fig. 2.— Examples of the best-fitting model spectra and the resulting stellar mass probability distribution as determined by the stellar mass code. The photometry points are plotted and final mass indicated. The dashed lines denote the 68% confidence intervals in the derived stellar mass.

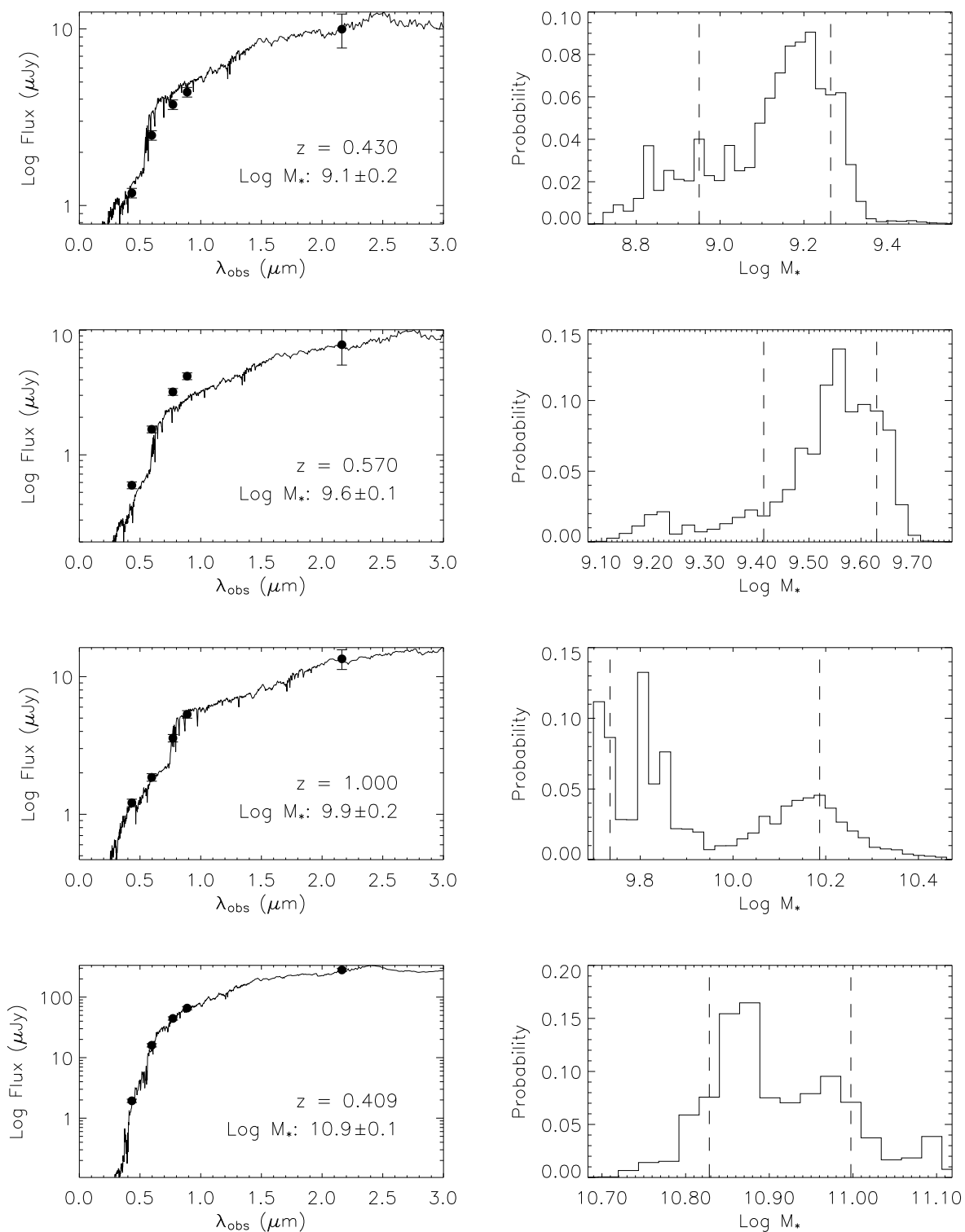


Fig. 3.— Difference in estimated stellar mass for our spectroscopic sample when photo-z’s are used instead of spec-z’s. The shaded region shows the expected standard deviation resulting from variations in the luminosity distance due to photo-z error.

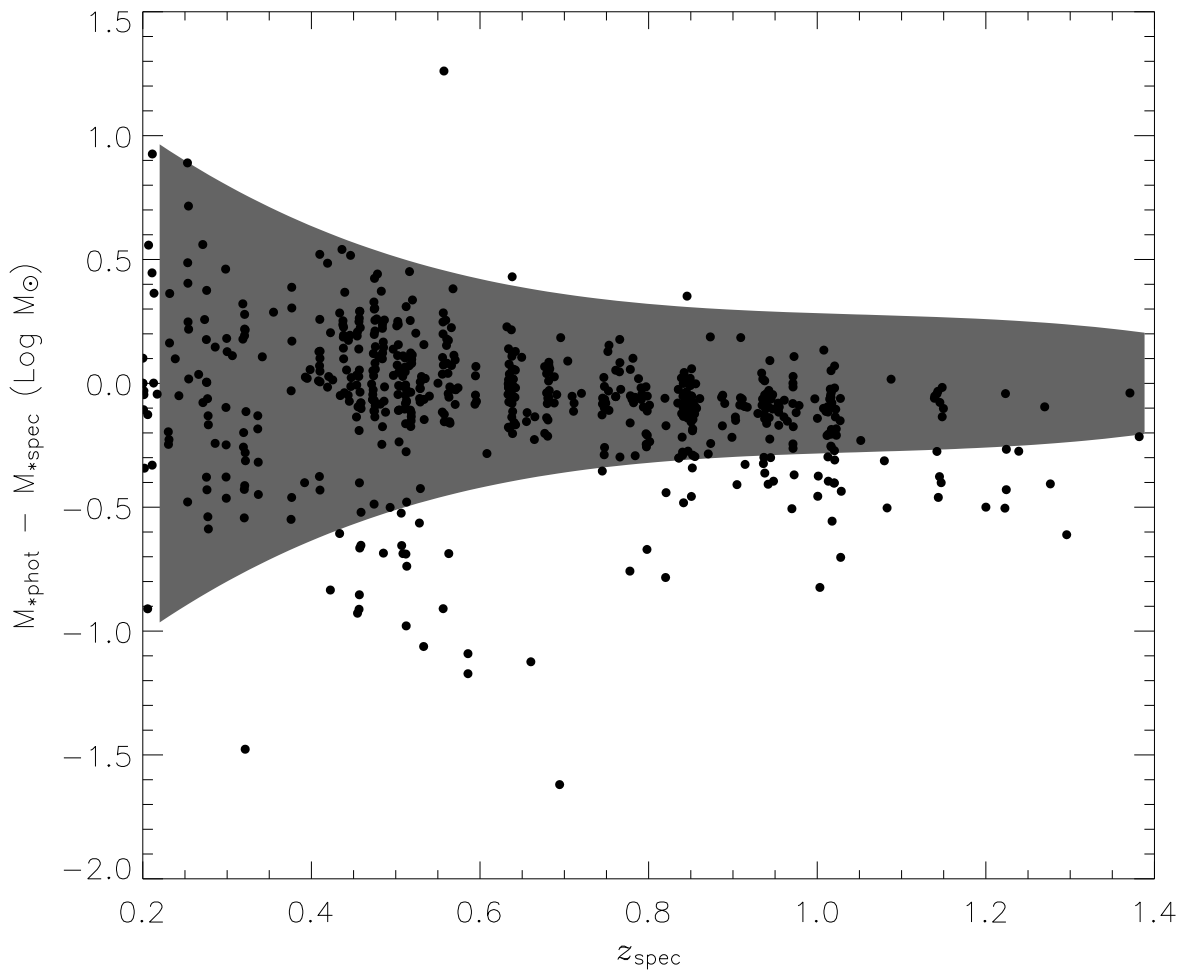


Fig. 4.— $(z - K_s)$ versus K_s color-magnitude relation. The small solid points are galaxies with spectroscopic redshifts. Open symbols denote those galaxies with photometric redshifts. The thin solid line illustrates the $z_{AB} < 22.5$ morphological classification limit, while the dotted line traces the completeness limit of the K_s -band data from Palomar and ESO. Three simple stellar population models, each with L_K^* luminosity and a formation redshift of $z_{form} = 10$, are also plotted. Models A and B have exponential SF timescales of $\tau = 0.4$ Gyr, and metallicities of $Z=0.05$ for A and $Z=0.02$ (Z_\odot) for B. Model C has $\tau = 4.0$ Gyr and solar metallicity. The large solid dots denote redshifts, from left to right, $z = 0.4, 0.8,$ and 1.2 .

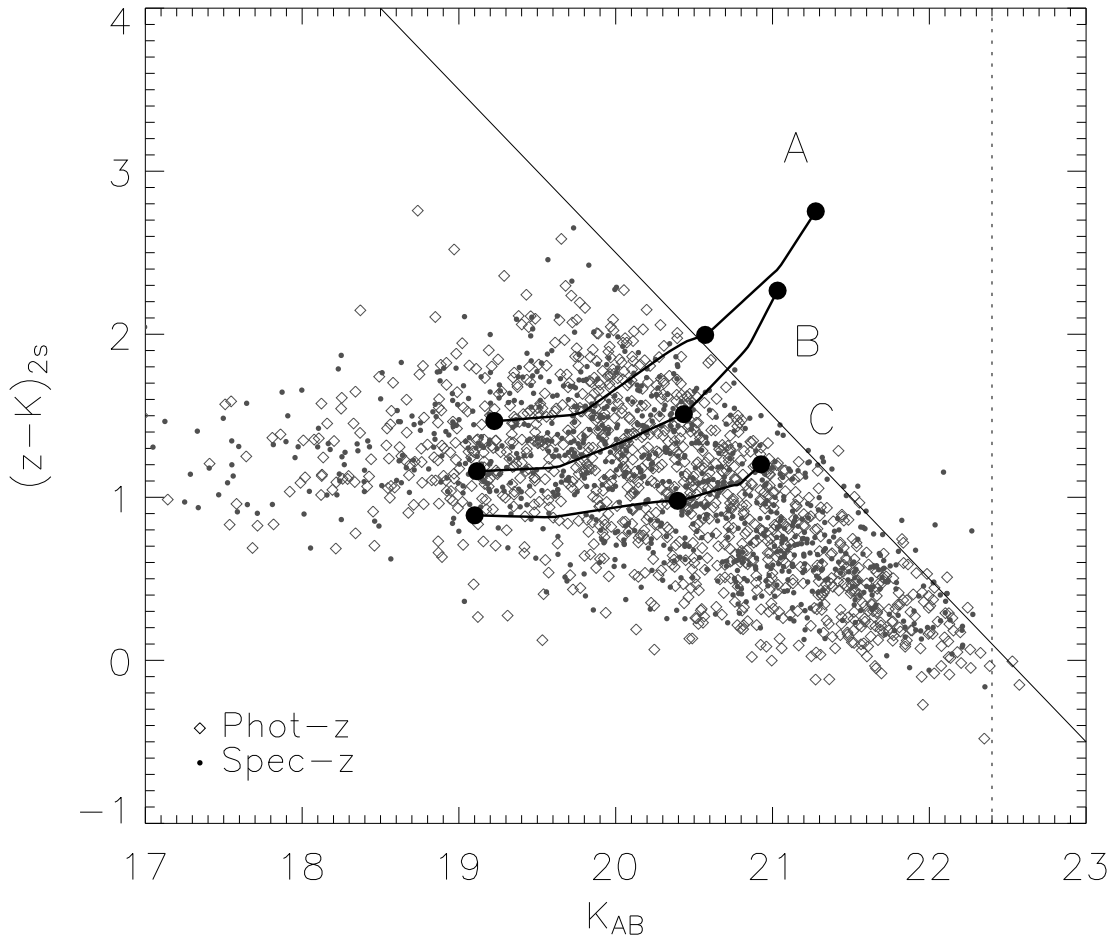


Fig. 5.— Redshift distributions for the primary GOODS sample with $z_{AB} < 22.5$.

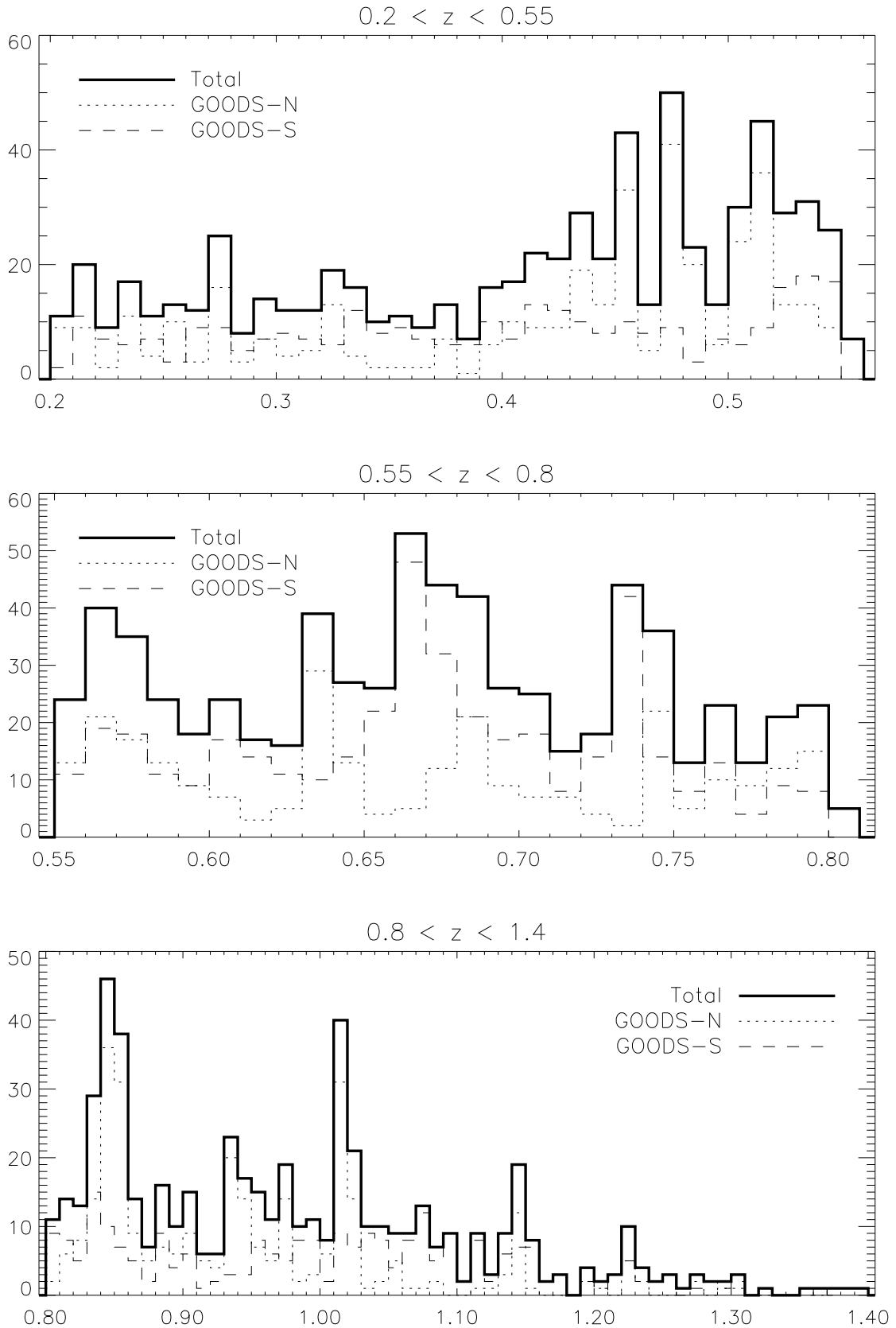


Fig. 6.— Total galaxy stellar mass functions in three redshift intervals. The solid line is the best fit to the $z = 0$ mass function from Cole et al. (2001). Results from Drory et al. (2004) and the “best-fit” stellar mass functions from Fontana et al. (2004) are shown, after correcting for different choices of the IMF and Hubble Constant. For the brighter, $z_{AB} < 22.5$ sample, mass completeness limits based on a maximum reasonable M_*/L_K ratio (see §4) are indicated by the dotted lines. The error bars are calculated from Monte Carlo simulations that account for uncertainties arising from the photometry, stellar mass estimates, photo- z estimates, and Poisson statistics.

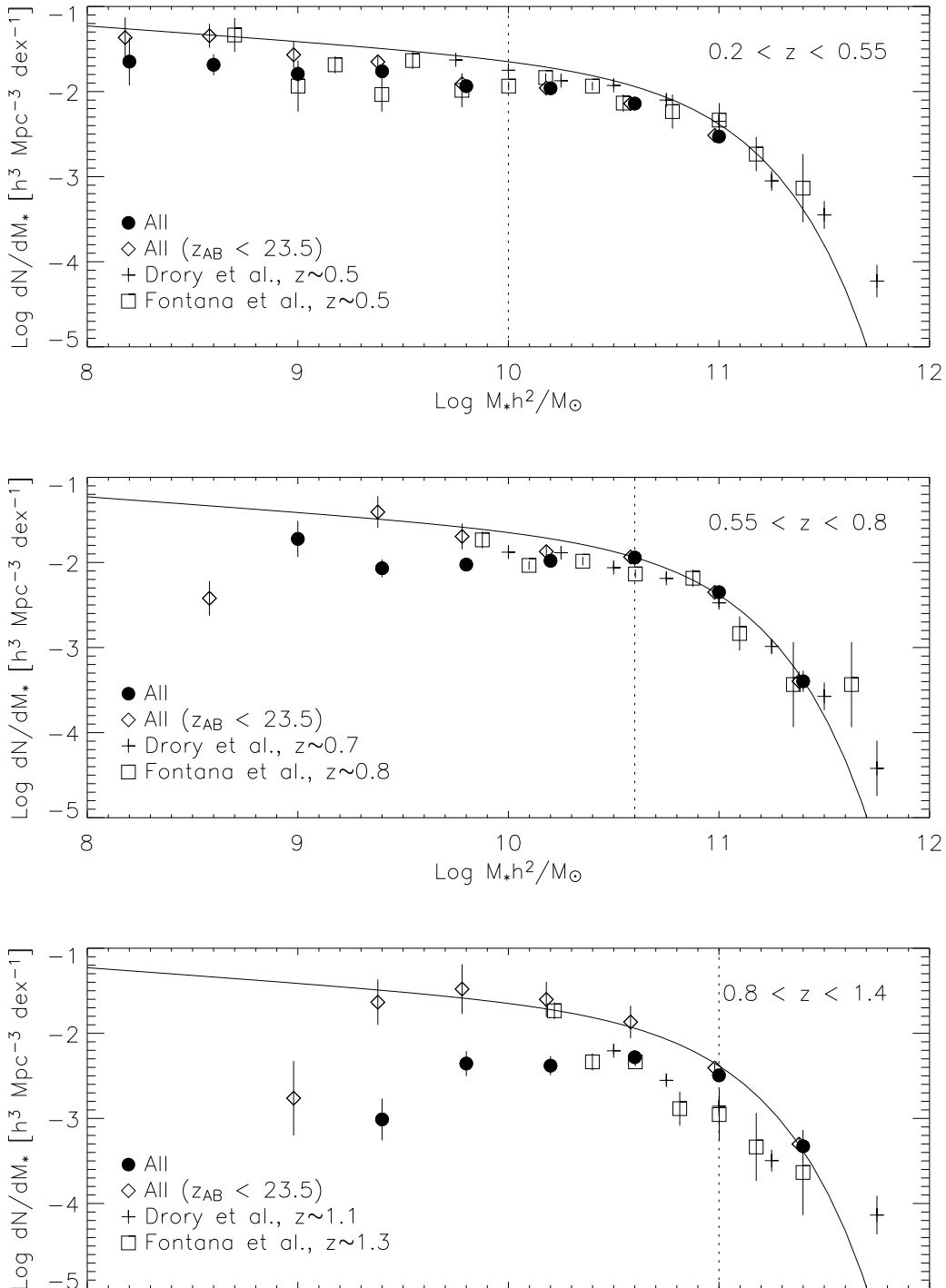


Fig. 7.— Galaxy stellar mass function in three redshift intervals split by morphology. The $z = 0$ mass function from Cole et al. (2001, solid line) and the total mass functions are also shown. Mass completeness limits based on a maximum reasonable M_*/L_K ratio (see §4) are indicated by the dotted lines. The error bars are calculated from Monte Carlo simulations that account for uncertainties arising from the photometry, stellar mass estimates, photo- z estimates, and Poisson statistics.

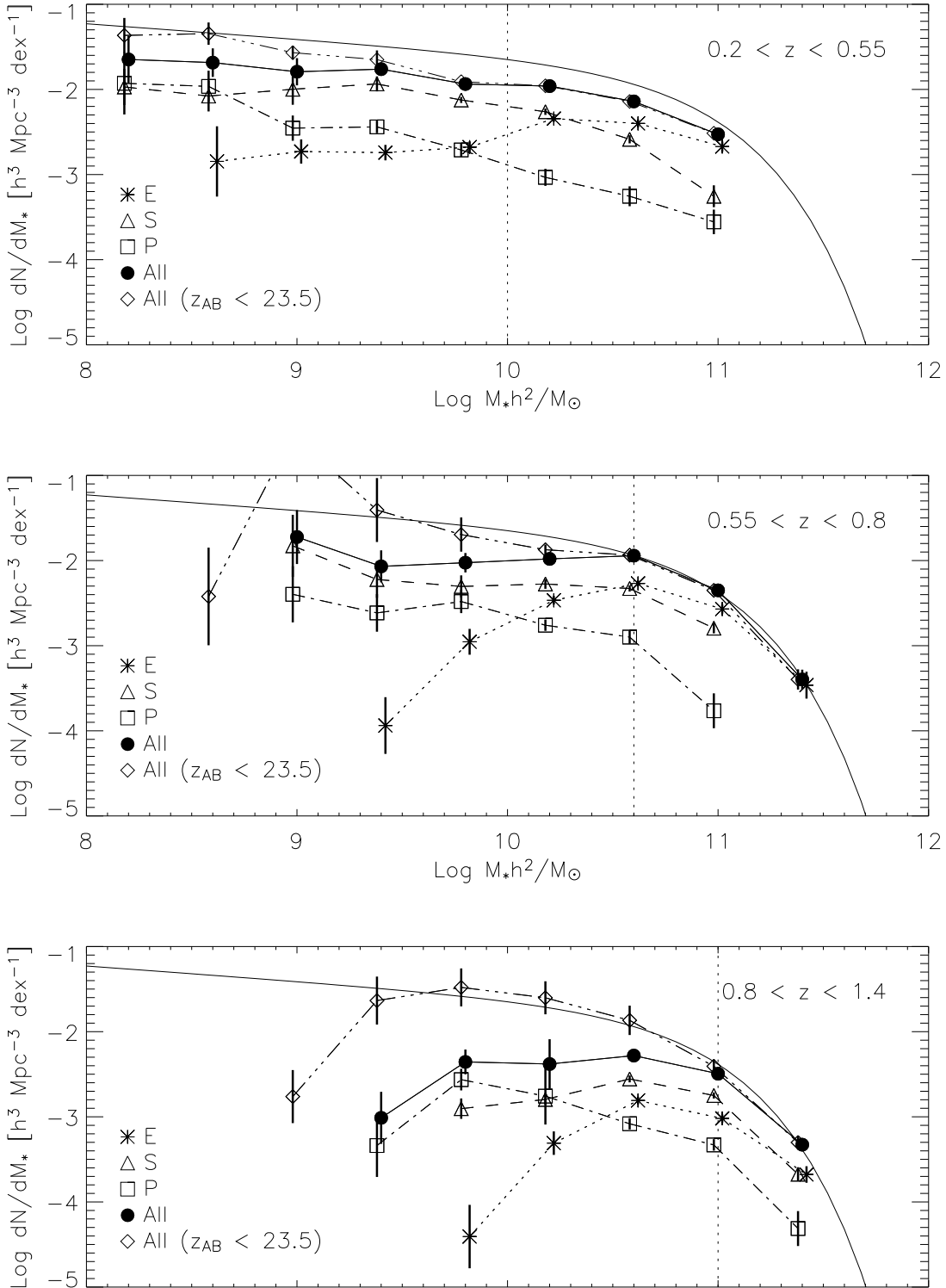


Fig. 8.— Integrated stellar mass density as a function of redshift, split by morphology and with a mass cut of $M_* > 10^{11} M_\odot$. The straight, solid line at the top of the plot shows the local stellar mass density as measured by Cole et al. (2001). The shaded region illustrates the uncertainty from cosmic variance.

